

1 **Impacts of an aerosol layer on a mid-latitude continental system of cumulus clouds:**  
2 **how do these impacts depend on the vertical location of the aerosol layer?**

3

4 Seoung Soo Lee<sup>1,2</sup>, Junshik Um<sup>3,4</sup>, Won Jun Choi<sup>5</sup>, Kyung-Ja Ha<sup>2,4,6</sup>, Chang Hoon Jung<sup>7</sup>,  
5 Jianping Guo<sup>8</sup>, Youtong Zheng<sup>9</sup>

6

7 <sup>1</sup>Earth System Science Interdisciplinary Center, University of Maryland, Maryland, USA

8 <sup>2</sup>Research Center for Climate Sciences, Pusan National University, Busan, Republic of  
9 Korea

10 <sup>3</sup>Department of Atmospheric Sciences, Pusan National University, Busan, Republic of  
11 Korea

12 <sup>4</sup>BK21 School of Earth and Environmental Systems, Pusan National University, Busan,  
13 Republic of Korea

14 <sup>5</sup>National Institute of Environmental Research, Incheon, Republic of Korea

15 <sup>6</sup>Center for Climate Physics, Institute for Basic Science, Busan, Republic of Korea

16 <sup>7</sup>Department of Health Management, Kyungin Women's University, Incheon, Republic of  
17 Korea

18 <sup>8</sup>State Key Laboratory of Severe Weather, Chinese Academy of Meteorological Sciences,  
19 Beijing, China

20 <sup>9</sup>The Program in Atmospheric and Oceanic Sciences, Princeton University, Princeton,  
21 New Jersey, USA

22

23

24

25 Corresponding authors: Seoung Soo Lee and Junshik Um

26 E-mail: [cumulss@gmail.com](mailto:cumulss@gmail.com), [slee1247@umd.edu](mailto:slee1247@umd.edu), [jjunum@pusan.ac.kr](mailto:jjunum@pusan.ac.kr)

27

28

29

30

31

32

33

34

35

36

37

38

39

40

41

42

43

44

45

46

47

48

49

50

51

**52 Abstract**

53

54 Effects of an aerosol layer on warm cumulus clouds in the Korean Peninsula when the layer  
55 is above or around the cloud tops in the free atmosphere are compared to those effects when  
56 the layer is around or below the cloud bases in the planetary boundary layer (PBL). For  
57 this comparison, simulations are performed using the large-eddy simulation framework.  
58 When the aerosol layer is in the PBL, aerosols absorb solar radiation and radiatively heat  
59 up air enough to induce greater instability, stronger updrafts and more cloud mass than  
60 when the layer is in the free atmosphere. Hence, there is a variation of cloud mass with the  
61 location (or altitude) of the aerosol layer. It is found that this variation of cloud mass  
62 reduces, as aerosol concentrations in the layer decrease or aerosol impacts on radiation are  
63 absent. The transportation of aerosols by updrafts reduces aerosol concentrations in the  
64 PBL. This in turn reduces the aerosol radiative heating, updraft intensity and cloud mass.

65

66

67

68

69

70

71

72

73

74

75

76

77

78

79

80

81

82

## 1. Introduction

Warm cumulus clouds play an important role in global hydrologic and energy circulations (Warren et al., 1986; Stephens and Greenwald, 1991; Hartmann et al., 1992; Hahn and Warren, 2007; Wood, 2012). Aerosols act as radiation absorbers, and they absorb solar radiation and heat up the atmosphere to change atmospheric stability. This in turn affects thermodynamics in cumulus clouds (Hansen et al., 1997). When these aerosols act as cloud condensation nuclei (CCN), they have an impact on aerosol activation and subsequent microphysical processes in cumulus clouds (Albrecht, 1989). However, these aerosol effects on warm cumulus clouds are highly uncertain and thus cause the highest uncertainty in the prediction of future climate (Ramaswamy et al., 2001; Forster et al., 2007).

In recent years, people have started to take interest in how aerosol layers affect clouds when these layers are above or around the tops of clouds (e.g., de Graaf et al., 2014; Xu et al., 2017). This interest is motivated by aerosol layers that are originated from biomass burning sites in the southern Africa (Mari et al., 2008; Menut et al., 2018; Haslett et al., 2019; Denjean et al., 2020). These layers are lifted and transported to the southeast Atlantic (SEA) region and located above or around the top of a large layer or deck of warm cumulus and stratocumulus clouds (Roberts et al., 2009; van der Werf et al., 2010; Che et al., 2022). Note that aerosols in the transported aerosol layers contain organic and black carbon, and these aerosols act as radiation absorbers as well as CCN (Wilcox, 2010; Deaconu et al., 2019; Chaboureau et al., 2022). Reflecting the interest, to better understand roles of aerosol layers above or around cloud tops in cloud development, there were international field campaigns in the SEA such as the National Aeronautics and Space Administration ObseRvations of Aerosols above CLouds and their intEractionS (ORACLES; <https://espo.nasa.gov/oracles/content/ORACLES>), the United Kingdom Clouds and Aerosol Radiative Impacts and Forcing (CLARIFY; Redemann et al., 2021) and the French Aerosol, Radiation and Clouds in southern Africa (AEROCLO-sA; Formenti et al., 2019) campaigns.

Despite above-mentioned field campaigns, effects of aerosols above or around tops of warm cumulus clouds, which are induced by shallow convection, have not been examined as much as those of aerosols around or below bottoms of those clouds (Haywood and Shine,

114 1997; Johnson et al., 2004; McFarquhar and Wang, 2006). Motivated by this, this study  
115 delves into effects of not only aerosols around or below bottoms of warm cumulus clouds  
116 but also those above or around tops of those clouds. Through this, this study aims to  
117 contribute to the more comprehensive understanding of aerosol-radiation-cloud  
118 interactions. This more comprehensive understanding in turn contributes to more general  
119 parameterizations of those interactions for climate and weather-forecast models. To fulfill  
120 the aim, this study adopts the large-eddy simulation (LES) framework and an idealized  
121 setup for the aerosol layer.

122

## 123 **2. Case, model and simulations**

124

### 125 **2.1 LES model**

126

127 The Advanced Research Weather Research and Forecasting (ARW) model is used for LES  
128 simulations in this study. The ARW adopts a 50-m resolution for the horizontal domain. In  
129 the vertical domain, the resolution coarsens with height. The resolution in the vertical  
130 domain is 20 m just above the surface and 100 m at the model top. The ARW model is a  
131 compressible model with a nonhydrostatic status. A 5th-order monotonic advection scheme  
132 is used to advect microphysical variables (Wang et al., 2009). The ARW adopts a bin  
133 scheme, which is detailed in Khain et al. (2011), to parameterize microphysics. A set of  
134 kinetic equations is solved by the bin scheme to represent size distribution functions for  
135 each class of hydrometeors and aerosols acting as cloud condensation nuclei (CCN). The  
136 hydrometeor classes are water drops, ice crystals (plate, columnar and branch types), snow  
137 aggregates, graupel and hail. There are 33 bins for each size distribution in a way that the  
138 mass of a particle  $m_j$  in the  $j$  bin is to be  $m_j = 2m_{j-1}$ .

139 Aerosol sinks and sources, which include aerosol advection and activation, control  
140 the evolution of aerosol size distribution at each grid point. For example, activated particles  
141 are emptied in the corresponding bins of the aerosol spectra. Aerosol mass included in  
142 hydrometeors, after activation, is moved to different classes and sizes of hydrometeors  
143 through collision-coalescence and removed from the atmosphere once hydrometeors that  
144 contain aerosols reach the surface.

145 The Rapid Radiation Transfer Model (RRTM; Mlawer et al., 1997) has been coupled  
146 to the bin microphysics scheme. Aerosols before their activation can affect radiation by  
147 changing the reflection, scattering, and absorption of radiation. This radiative effect of  
148 aerosol is represented following Feingold et al. (2005). The internal aerosol mixture and  
149 the ARW relative humidity are used to calculate the hygroscopic growth of the aerosol  
150 particles as well as their optical properties. In practice, optical property calculations with  
151 the consideration of the hygroscopic growth are performed offline prior to simulation and  
152 stored in lookup tables. Calculations are done for the prescribed aerosol size distribution  
153 and composition, and unit concentration. During model runtime, grid-point number  
154 concentration and relative humidity determine the look-up table entries that specify the  
155 grid-point aerosol optical properties and are fed into the RRTM to simulate the radiative  
156 effect of aerosol. The effective sizes of hydrometeors are calculated in the bin scheme and  
157 the calculated sizes are transferred to the RRTM to consider effects of the effective sizes  
158 on radiation.

159 The presence of aerosol perturbs the radiative fluxes reaching the surface, and its  
160 subsequent partitioning into sensible and latent heat fluxes (i.e., the Bowen ratio). This is  
161 accounted for with the interactive Noah land surface model (Chen and Dudhia, 2001).

162

## 163 **2.2 Case and simulations**

164

### 165 **2.2.1 Case and standard simulations**

166

167 As a case study, we simulate an observed system of warm cumulus clouds in a domain in  
168 the Korean Peninsula on April 13<sup>th</sup>, 2016. The domain is marked in Figure 1a. Figure 2  
169 shows the field of the cloud reflectivity observed by the Communication, Ocean, and  
170 Meteorological Satellite (COMS). This field is at 14:00 LST on April 13<sup>th</sup>, 2016 when the  
171 system is around the mature stage in the domain. The ratio of the reflected radiative flux  
172 by an object to the incident radiative flux on it is the reflectivity (Liou, 2002) and thus  
173 unitless. In Figure 2, we see cloud cells that are elongated in the southwest-northeast  
174 direction due to the southwesterly wind.

175 The simulation is performed for a period between 10:00 and 18:00 LST on April 13<sup>th</sup>,  
176 2016. This period includes a time span over which the system exists. For the simulation  
177 (i.e., the control run), the length of the domain in both the east-west and north-south  
178 directions is 20 km and the model top is at ~4.5 km in altitude. The time step or temporal  
179 resolution is set at 0.1 second. Initial and boundary conditions of potential temperature,  
180 specific humidity, and wind for the simulation are provided by reanalysis data. These data  
181 represent the synoptic-scale environment and are produced by the Met Office Unified  
182 Model (Brown et al., 2012) every 6 hours on a  $0.11^\circ \times 0.11^\circ$  grid. Figure 3 depicts the  
183 vertical distributions of potential temperature and water-vapor mixing ratio at 09:00 LST  
184 on April 13<sup>th</sup>, 2016 in radiosonde sounding that is obtained near the domain as marked in  
185 Figure 1a. This vertical distribution represents initial environmental conditions for the  
186 control run. The conditional instability is present in the vertical profiles and this favors the  
187 development of warm cumulus clouds. An open lateral boundary condition is employed  
188 for the run.

189 Not only a site of the aerosol robotic network (AERONET; Holben et al., 2001) but  
190 also ground stations that measure  $PM_{2.5}$  are in the domain as marked in Figure 1b. The mass  
191 of aerosols with diameter smaller than  $2.5 \mu\text{m}$  per unit volume of the air is  $PM_{2.5}$ . Around  
192 07:00 LST on April 13<sup>th</sup>, 2016, an aerosol layer advected from East Asia starts to be present  
193 in the domain. This advection of aerosols is monitored and identified by  $PM_{2.5}$  which is  
194 measured by stations in the Yellow sea and domain (Eun et al., 2016; Ha et al., 2019; Lee  
195 et al., 2021). The station in the Yellow sea is marked in Figure 1a. Figure 4 shows the  
196 evolution of  $PM_{2.5}$  at the station in the Yellow sea and the average  $PM_{2.5}$  over stations in  
197 the domain from 03:00 LST to 18:00 LST on April 13<sup>th</sup>, 2016. Due to the aerosol-layer  
198 advection from East Asia, aerosol mass starts to increase around 04:00 LST and reaches its  
199 peak around 08:00 LST at the station in the sea. Then, in the domain, aerosol mass starts  
200 to increase around 07:00 LST, and the mass attains its peak around 11:00 LST. This depicts  
201 a situation where aerosols or an aerosol layer advected from East Asia first arrives at the  
202 station in the Yellow sea around 04:00 LST and then further advected to the east to reach  
203 the domain and to start the increase in aerosol mass there around 07:00 LST.

204 According to the AERONET measurement at 12:00 LST, which is ~1 hour before  
205 the observed cumulus clouds start to form, aerosol particles in the advected aerosol layer,

206 on average, are an internal mixture of 70 % ammonium sulfate, 22 % organic compound  
207 and 8% black carbon. Aerosol chemical composition in this study is assumed to be  
208 represented by this mixture in the whole domain during the whole simulation period. Based  
209 on the AERONET observation, the shape of the initial size distribution of aerosols acting  
210 as CCN is assumed to follow a bi-modal log-normal distribution as shown in Figure 5 in  
211 all parts of the domain. Modal radius of this distribution is 0.11 and 1.20  $\mu\text{m}$  and standard  
212 deviation of this distribution is 1.71 and 1.92, while the partition of aerosol number, which  
213 is normalized by the total aerosol number of the size distribution, is 0.999 and 0.001 for  
214 accumulation and coarse modes, respectively. The total aerosol number concentration in  
215 the advected aerosol layer based on the AERONET-observed size distribution is  $\sim 15000$   
216  $\text{cm}^{-3}$ . This concentration is applied to all grid points in the aerosol layer at the first time  
217 step of the control run. This aerosol layer is idealized to be located around or below cloud  
218 bases between the surface and 1.0 km in the planetary boundary layer (PBL). Cloud bases  
219 are located around 1.0 km. At 06:00 LST,  $\sim 1$  hour before the advected aerosol layer starts  
220 to be present, the AERONET-measured aerosol concentration is  $\sim 150 \text{ cm}^{-3}$  in the domain.  
221 This aerosol concentration is assumed to be a background aerosol concentration that is not  
222 affected by the advected aerosol layer. Based on this assumption, the initial aerosol  
223 concentration is set at  $150 \text{ cm}^{-3}$  outside the layer.

224 This study compares aerosol effects on warm cumulus clouds when the aerosol layer  
225 is above or around the cloud tops to those effects when the layer is around or below the  
226 cloud bases. For this, we repeat the control run by moving the aerosol layer upward to  
227 altitudes between 2.5 and 3.5 km in the free atmosphere which is above the PBL. Here,  
228 initial aerosol concentrations in and outside the aerosol layer are  $15000 \text{ cm}^{-3}$  and  $150 \text{ cm}^{-3}$ ,  
229 respectively, in both of the runs. Altitudes between 2.5 and 3.5 km are places where cloud  
230 tops are located frequently and the simulated maximum cloud-top height is 3.3 km. This  
231 repeated run is referred to as the aro-above-cld run.

232 It is well-known that aerosol-cloud-radiation interactions are strongly dependent on  
233 aerosol concentrations (Tao et al., 2012). Hence, we want to test how results in the control  
234 and aro-above-cld runs are sensitive to aerosol concentrations in the aerosol layer. For the  
235 test, the control and aro-above-cld runs are repeated with 10 times lower initial aerosol  
236 concentrations in the aerosol layer but with no changes in initial aerosol concentrations



237 outside the layer. In these repeated runs, the aerosol concentration in the aerosol layer at  
238 the first time step is  $1500 \text{ cm}^{-3}$ . Henceforth, the repeated control and aro-above-cld runs  
239 are referred to as the control-1500 and aro-above-cld-1500 runs.

240

### 241 **2.2.2 Additional simulations**

242

243 Clouds affect aerosols through cloud processes such as nucleation of droplets and aerosol  
244 transportation (or advection) by cloud-induced wind. Updrafts and downdrafts comprise  
245 cloud-induced wind and transport aerosols upward and downward, respectively. Motivated  
246 by this, we take interest in impacts of clouds on aerosols and how these impacts in turn  
247 change the influence of aerosols on clouds. To examine this aspect of aerosol-cloud  
248 interactions, the above-mentioned four standard simulations (i.e., the control, aro-above-  
249 cld, control-1500 and aro-above-cld-1500 runs) are repeated. In these repeated runs,  
250 aerosol concentrations at each grid point, which are set at the first time step, do not vary  
251 with time or are not affected by cloud processes. These repeated runs are referred to as the  
252 control-novary, aro-above-cld-novary, control-1500-novary, and aro-above-cld-1500-  
253 novary runs. By comparing the standard simulations to these repeated ones, we aim to  
254 identify how cloud processes affect the aerosol layer and then the impacts of the layer on  
255 clouds.

256 In this study, we also aim to better understand roles of the interception (e.g., reflection,  
257 scattering and absorption) of radiation by aerosols in impacts of the aerosol layer on clouds.  
258 This interception of radiation by aerosols, which is referred to as aerosol radiative effects,  
259 results in phenomena such as radiative heating of air by aerosols. To better understand roles  
260 of aerosol radiative effects, the above four standard simulations are repeated again by  
261 turning off aerosol radiative effects. These repeated runs are the control-norad, aro-above-  
262 cld-norad, control-1500-norad, aro-above-cld-1500-norad runs. The summary of  
263 simulations in this study is given in Table 1.

264

## 265 **3. Results**

266

### 267 **3.1 The control and aro-above-cld runs**

268

269 Figure 6 depicts the simulated field of the cloud reflectivity at 14:00 LST on April 13<sup>th</sup>,  
270 2016 in the control run. Similar to the observed counterpart in Figure 2, simulated cloud  
271 cells are elongated in the southwest-northeast direction. Also, there is a good consistency  
272 in the overall cell size and population and the overall pattern of the spatial distribution of  
273 cloud cells between the observed and simulated fields. Table 3 shows comparisons of cloud  
274 and environmental variables between observation and the control run. Observation is  
275 performed by ground stations and satellites. Note that ground stations which measure PM<sub>2.5</sub>  
276 as marked in Figure 1b also measure cloud and environmental variables. Table 3 shows  
277 that differences in those variables between observation and the control run are ~10%. This  
278 and Figure 6 indicate that the control run can be considered performed reasonably well.

279 Figure 7 shows the time- and area-averaged vertical distributions of cloud-liquid mass  
280 density for the standard simulations. In Figure 7, the cloud layer is between 1.0 and 3.3 km  
281 in the control run and between 0.8 and 2.6 km in the aro-above-cld run. The time- and  
282 domain-averaged cloud-liquid mass density is  $0.7$  and  $1.3 \times 10^{-3}$  g m<sup>-3</sup> in the control run  
283 and in the aro-above-cld run, respectively. Hence, we see that clouds are thicker with their  
284 higher tops and have greater mass in the control run than in the aro-above-cld run.

285 Figure 8a shows the time series of the domain-averaged liquid-water path, which is  
286 the vertical integral of cloud-liquid mass density, for the standard simulations. During the  
287 initial stage of the cloud development between 12:50 and 13:50 LST, the average cloud  
288 mass is slightly higher in the control run than in the aro-above-cld run. Also, the average  
289 non-zero cloud mass starts to appear earlier in the control run. Over the period between  
290 13:50 and 14:10 LST, there is a jump (or rapid increase or surge) in the average cloud mass  
291 in the control run but not in the aro-above-cld run. During this period with the jump, at  
292 some specific time points, the average mass is ~one order of magnitude higher in the  
293 control run. Of interest is that just after the jump and at 14:10 LST, the average mass in the  
294 control run starts to decrease and at 14:40 LST, becomes lower than that in the aro-above-  
295 cld run. Hence, the greater time- and domain-averaged cloud mass in the control run is  
296 mainly attributed to the jump. Figures 8b and 8c show the time series of the domain-  
297 averaged updraft speed and condensation rates, respectively. These figures indicate that the  
298 average updraft mass fluxes and associated condensation rates in the control run are also

299 slightly higher than in the aro-above-cld run for the period between 12:50 and 13:50 LST.  
300 The average updraft speed and associated condensation rates jump and thus are much  
301 higher in the control run during the period between ~13:50 and ~14:10 LST (Figures 8b  
302 and 8c). After the jump, the speed and rates decrease rapidly and become lower in the  
303 control run (Figures 8b and 8c). Condensation is the only source of cloud mass in warm  
304 cumulus clouds. Also, updrafts with higher speeds tend to produce higher condensation  
305 rates for a given environmental condition. Hence, cloud mass, condensation rate and the  
306 updraft speed are closely linked to each other. This enables cloud mass, condensation rate  
307 and the updraft speed to be similar in terms of their temporal evolution in each of the  
308 control and aro-above-cld runs (Figures 8a, 8b and 8c).

309 Figure 8d shows the time series of the domain-averaged convective available potential  
310 energy (CAPE) for the control and aro-above-cld runs. Considering that updrafts grow by  
311 consuming buoyancy energy, updraft intensity is proportional to CAPE that is the integral  
312 of the buoyancy energy in the vertical domain. Hence, the evolution of CAPE is similar to  
313 that of the updraft speed, associated condensation rates and cloud mass (Figure 8). This  
314 involves the jump not only in CAPE but also in those speed, rates and mass in the control  
315 run.

316 In Figure 8, the peaks (or the maximum values) of the domain-averaged CAPE, the  
317 updraft speed, condensation rates and cloud mass in the control run occur around 14:10  
318 LST and this occurrence is earlier than that which occurs around 14:50 LST in the aro-  
319 above-cld run. This means that the cloud system in the control run reaches its mature stage  
320 earlier. Immediately after the peak around 14:10 LST, the system enters its dissipating  
321 stage in the control run. However, the system enters its dissipating stage after 14:50 LST  
322 in the aro-above-cld run. Hence, the cloud system in the control run matures and demises  
323 faster. Stated differently, the cloud system in the control run has a shorter life cycle.

324 To find mechanisms controlling the jump in CAPE which is a main cause of the greater  
325 cloud mass in the control run, the analysis of the results is done for an initial period between  
326 10:00 LST and 13:50 LST which is immediately before the jump starts to occur. The  
327 average net shortwave fluxes at the surface are shown in Table 2 for the initial period in  
328 the control and aro-above-cld runs. Table 2 shows that during the initial period, there is a  
329 smaller amount of the surface-reaching shortwave radiation in the control run than in the

330 aro-above-cld run. The aerosol layer intercepts solar radiation and reduces the surface-  
331 reaching solar radiation. In spite of the fact that the initial depth of the aerosol layer and  
332 aerosol concentrations in the layer are identical between the runs, results here indicate that  
333 the aerosol layer in the atmosphere around or below cloud bases is more efficient in the  
334 interception of solar radiation than that in the atmosphere around or above cloud tops. Due  
335 to the less solar radiation reaching the surface, the time- and area-averaged net surface heat  
336 fluxes, which are the sum of the surface sensible and latent-heat fluxes, become lower in  
337 the control run during the initial period (Table 2). Hence, the surface fluxes favor more  
338 instability or higher CAPE and associated subsequent more intense updrafts and more  
339 cloud mass in the aro-above-cld run.

340 The vertical distributions of the time- and domain-averaged radiative heating rates are  
341 obtained for the initial period. For the initial period, the average radiative heating rate is  
342 much higher in the control run than in the aro-above-cld run particularly at altitudes  
343 between 0.0 and  $\sim 1.0$  km where cloud bases are located (Figure 9a). This is associated with  
344 the fact that the aerosol layer is located at altitudes between 0.0 and 1.0 km in the control  
345 run. This more radiative heating in the PBL during the initial period results in the  
346 subsequent jump in CAPE, associated higher CAPE, more intense updrafts and more cloud  
347 mass after the initial period by outweighing the lower surface heat fluxes in the control run.  
348 The aerosol layer is located at altitudes between 2.5 and 3.5 km, hence, the average  
349 radiative heating rate is higher around those altitudes in the aro-above-cld run (Figures 9a  
350 and 9b). However, this higher radiative heating rate is in the upper part of the domain and  
351 tends to induce more stabilization of the atmosphere in the aro-above-cld run. Thus, the  
352 higher radiative heating rate in the aro-above-cld run contributes to lower CAPE, less  
353 intense updrafts and less cloud mass in the aro-above-cld run especially for the period when  
354 the jumps occur in the control run.

355

### 356 **3.2 Comparisons between simulations with different aerosol concentrations**

357

358 With the lower concentration of aerosols in the aerosol layer, there are the much more  
359 surface-reaching solar radiation and resultant higher surface fluxes in the control-1500 run  
360 than in the control run and in the aro-above-cld-1500 run than in the aro-above-cld run

361 (Table 2). This induces higher CAPE, stronger updrafts and more condensation and cloud  
362 mass in the control-1500 run than in the control run over most of the simulation period  
363 except for the period with the jump in CAPE in the control run, and in the aro-above-cld-  
364 1500 run than in the aro-above-cld run throughout the simulation period (Figure 8). This  
365 leads to the greater time- and domain-averaged cloud mass in the control-1500 run than in  
366 the control run and in the aro-above-cld-1500 run than in the aro-above-cld run (Figure 7).  
367 Regarding the control and control-1500 runs, this is despite the fact that aerosol radiative  
368 heating in the PBL is higher due to higher aerosol concentrations there in the control run  
369 than in the control-1500 run (Figure 9). Regarding the aro-above-cld-1500 and the aro-  
370 above-cld runs, the greater time- and domain-averaged cloud mass is contributed by lower  
371 aerosol concentrations and less aerosol radiative heating in the free atmosphere in the aro-  
372 above-cld-1500 run than in the aro-above-cld run (Figure 9). Figure 7 shows that the time-  
373 and domain-averaged cloud mass in the aro-above-cld-1500 run is higher than in the  
374 control run. This is due to more solar radiation reaching the surface in the aro-above-cld-  
375 1500 run (Table 2). The higher average cloud mass in the aro-above-cld-1500 run is despite  
376 higher aerosol concentrations and more aerosol radiative heating not only in the PBL in the  
377 control run, but also in the free atmosphere in the aro-above-cld-1500 run (Figure 9). Figure  
378 7 also shows that the time- and domain-averaged cloud mass in the control-1500 run is  
379 higher than in the aro-above-cld run. This is associated with the fact that more solar  
380 radiation reaches the surface in the control-1500 run than in the aro-above-cld run (Table  
381 2). The higher average cloud mass in the control-1500 run is also associated with higher  
382 aerosol concentrations and more aerosol radiative heating not only in the PBL in the  
383 control-1500 run, but also in the free atmosphere in the aro-above-cld run (Figure 9).

384 Similar to the situation between the control and aro-above-cld runs, there is the less  
385 surface-reaching solar radiation in the control-1500 run than in the aro-above-cld-1500 run  
386 (Table 2). In association with this, there is the less surface heat fluxes in the control-1500  
387 run. However, overall, CAPE is higher and cloud mass is greater in the control-1500 run  
388 than in the aro-above-cld-1500 run (Figures 7, 8a and 8d). This is because similar to the  
389 situation between the control and aro-above-cld runs, aerosols heat up the PBL more in the  
390 control-1500 run and the free atmosphere more in the aro-above-cld-1500 run (Figure 9c).  
391 The CAPE evolution shows that there is no jump in CAPE and thus updrafts in the control-

392 1500 run (Figures 8b and 8d). This mainly contributes to smaller differences in CAPE,  
393 updrafts, condensation and cloud mass between the control-1500 and aro-above-cld-1500  
394 runs than between the control and aro-above-cld runs (Figures 7 and 8).

395 In the control run, the instability or CAPE accumulates or increases rapidly to reach  
396 its peak for a period between 13:50 and 14:10 LST, while in the control-1500 run, CAPE  
397 increases gradually to reach its peak from ~12:00 LST to ~14:30 LST (Figure 8d). For a  
398 period between ~14:10 and ~14:50 LST, CAPE reduces rapidly down back to the CAPE  
399 value around ~13:50 LST in the control run. However, CAPE decreases gradually and  
400 never drops back to the CAPE value at ~12:00 LST until the end of the simulation period  
401 in the control-1500 run. This leads to the shorter life cycle or lifetime of the system in the  
402 control run than in the control-1500 run as well as in the aro-above-cld run. Accompanying  
403 this is the similar life cycle between the control-1500 and aro-above-cld-1500 runs. Here,  
404 we see that as aerosol concentration increases in the aerosol layer in the atmosphere around  
405 or below cloud bases, the time scale of the accumulation and consumption of the instability  
406 or convective energy gets shorter, leading to the shorter lifetime of the cloud system.

407

### 408 **3.3 Comparisons between simulations with predicted and prescribed aerosol** 409 **concentrations**

410

411 Figure 10 shows the vertical distributions of aerosol concentrations, which are averaged  
412 over the horizontal domain and simulation period, for the standard and repeated runs with  
413 no temporal variation of aerosols. Comparisons between the control and control-novary  
414 runs and between the control-1500 and control-1500-novary runs show that due to the  
415 upward transportation of aerosols by updrafts, aerosol concentrations in the aerosol layer  
416 in the PBL reduces and those in the air above the layer increases (Figures 10a and 10c).  
417 Note that the PBL is where cloud-induced updrafts develop and grow, hence, the upward  
418 transportation of aerosols by them is dominant. This leads to the more PBL radiative  
419 heating of air by aerosols in the control-novary run than in the control run and in the  
420 control-1500-novary run than in the control-1500 run.

421 Comparisons between the aro-above-cld and aro-above-cld-novary runs and between  
422 the aro-above-cld-1500 and aro-above-cld-1500-novary runs show that due to the

423 transportation of aerosols by downdrafts, aerosol concentrations in the aerosol layer in the  
424 free atmosphere reduces and those in the air below the layer increases (Figures 10b and  
425 10d). Note that the free atmosphere, which includes the above-PBL atmosphere around or  
426 above cloud tops, is where cloud-induced updrafts decelerate and turn into downdrafts, and  
427 the downward transportation of aerosols by them is dominant. However, those increases in  
428 aerosol concentrations in the air below the aerosol layer mainly occur between  $\sim 1.5$  and  
429  $\sim 2.5$  km, and aerosol concentrations and the associated instability in the PBL do not change  
430 significantly (Figures 10b and 10d). This leads to similar instability in the PBL and CAPE,  
431 which in turn leads to similar updrafts and cloud mass between the aro-above-cld and aro-  
432 above-cld-novary runs and between the aro-above-cld-1500 and aro-above-cld-1500-  
433 novary runs (Figure 11a).

434 Due to more radiative heating of air in the PBL, there are higher CAPE, stronger  
435 updrafts and higher cloud mass in the control-novary run than in the control run and in the  
436 control-1500-novary run than in the control-1500 run (Figure 11a). It is notable that cloud  
437 mass in the control-novary run is so large that its maximum value in the vertical profile  
438 exceeds that even in the control-1500-novary run (Figure 11a). Associated with this, there  
439 are only  $\sim 20$  % changes in cloud mass between the control-1500 and control-1500-novary  
440 runs, while there are as much as  $\sim 200$  % changes in cloud mass between the control and  
441 control-novary runs. This indicates that with higher aerosol concentrations in the PBL,  
442 changes in cloud mass due to the wind-induced variation of those concentrations are much  
443 larger.

444

### 445 **3.4 Comparisons between simulations with and without aerosol radiative effects**

446

447 Figure 11b shows that with no aerosol radiative effects, differences in cloud mass due to  
448 the altitude of the aerosol layer are smaller. However, even with no aerosol radiative effects,  
449 there is higher cloud mass when the aerosol layer is in the PBL than in the free atmosphere  
450 as in the standard runs. Also, cloud mass increases when aerosol radiative effects are turned  
451 off and this increase enhances as aerosol concentrations increase (Figure 11b). Here, we  
452 see that aerosol radiative effects suppress clouds and reduce cloud mass by reducing the  
453 surface-reaching solar radiation and the surface heat fluxes. The suppression of clouds and

454 reduction in cloud mass are greater with higher aerosol concentrations, since more aerosols  
455 reduce the surface-reaching solar radiation more.

456 Note that aerosol activation mainly occurs around cloud bases in the PBL and more  
457 aerosols induce more activation for a given thermodynamic condition. Hence, there are  
458 more aerosol activation (or nucleation of droplets) and higher cloud droplet number  
459 concentration (CDNC) when the aerosol layer is in the PBL than in the free atmosphere.  
460 The averaged CDNC over grid points with non-zero CDNC and the whole simulation  
461 period is 532, 57, 131 and 53  $\text{cm}^{-3}$  in the control-norad, aro-above-cld-norad, control-1500-  
462 norad and the aro-above-cld-1500-norad runs, respectively. Droplets act as a source of  
463 condensation, since individual droplets provide their surface areas onto which water vapor  
464 condenses. Hence, higher CDNC induces more condensation and this in turn induces  
465 stronger updrafts and more cloud mass with the aerosol layer in the PBL than in the free  
466 atmosphere. These effects of more aerosols, which induce more condensation and stronger  
467 updrafts, are generally referred to as aerosol microphysical effects (Lee et al., 2016). The  
468 differences in CDNC due to the altitude of the aerosol layer increase with increasing  
469 aerosol concentrations. This leads to greater differences in condensation, associated  
470 updrafts and cloud mass due to the altitude of the aerosol layer with higher aerosol  
471 concentrations when there are no aerosol radiative effects (Figure 11b).

472 Here, we see that differences in cloud mass due to the altitude of the aerosol layer are  
473 greater when aerosol microphysical and radiative effects work together than when aerosol  
474 microphysical effects work alone (Figure 11b). Also, remember that the initial  
475 concentration of aerosols in the aro-above-cld-norad run is identical to that in the aro-  
476 above-cld-1500-norad run in the PBL. Due to this, CDNC, condensation and cloud mass  
477 in the aro-above-cld-norad run are similar to those in the aro-above-cld-1500-norad run  
478 (Figure 11b).

479

#### 480 **4. Summary and conclusions**

481

482 This study examined how impacts of aerosols on warm cumulus clouds in the Korean  
483 Peninsula vary with the altitude of an aerosol layer. It is found that the aerosol layer  
484 intercepts the surface-reaching solar radiation more when the layer is in the PBL, which



485 corresponds to the atmosphere around or below cloud bases, than in the free atmosphere  
486 which includes the above-PBL atmosphere around or above cloud tops. With the aerosol  
487 layer in the PBL, this makes the surface heat fluxes and associated CAPE lower, which  
488 tend to make updrafts weaker and cloud mass lower. However, the layer in the PBL heats  
489 up the air there more to produce the higher CAPE and cloud mass.

490 With decreasing concentrations of aerosols in the aerosol layer, there are decreases in  
491 the interception of the surface-reaching solar radiation, increases in surface heat fluxes,  
492 CAPE and cloud mass. However, the decreasing concentrations of aerosols cause the jump  
493 in CAPE to disappear when the layer is in the PBL. This makes differences in cloud mass  
494 due to the altitude of the layer reduce. When the aerosol layer is in the PBL, with increasing  
495 aerosol concentrations in the layer, the lifetime of cloud system reduces and becomes  
496 shorter than when the layer is in the free atmosphere.

497 Updrafts and downdrafts in clouds transport aerosols. In particular, for the aerosol layer  
498 in the PBL, updrafts transport aerosols in the layer to places above it. This reduces aerosol  
499 concentrations in the layer, leading to reduction in radiative heating of air by aerosols,  
500 CAPE, updrafts and cloud mass. This reduction enhances with increasing aerosol  
501 concentrations in the layer. For the aerosol layer in the free atmosphere, downdrafts  
502 transport aerosols in the layer to places below it. However, this does not affect aerosol  
503 concentrations and radiative heating of air in the PBL significantly. This in turn has  
504 negligible effects on CAPE and cloud mass.

505 Aerosol radiative effects suppress clouds and reduce cloud mass by cutting down the  
506 surface-reaching solar radiation. This suppression of clouds increases with increasing  
507 aerosol concentrations in the aerosol layer. Aerosol microphysical effects enhance cloud  
508 mass and these effects are stronger with higher aerosol concentrations. Differences in cloud  
509 mass due to the altitude of the aerosol layer are enhanced when aerosol radiative effects  
510 and aerosol microphysical effects work together as compared to when only aerosol  
511 microphysical effects are present.

512 This study shows that aerosol-induced changes in the surface fluxes and those in  
513 radiative heating of air interact with each other in terms of responses of convection and  
514 clouds to aerosols. This interaction varies with the altitude of aerosols and cloud-induced  
515 wind. In general, traditional parameterizations for warm cumulus clouds in climate and

516 weather-forecast models have not been able to consider this dependence of the interaction  
517 on the altitude of aerosols, since those parameterizations do not differentiate aerosol layers  
518 based on their vertical locations. In addition, the cloud-induced wind at cloud scales has  
519 not been represented by those parameterizations with good confidence. So, impacts of  
520 aerosol transportation by cloud-induced wind on the interaction have not been properly  
521 considered in those traditional parameterizations. This suggests that the vertical locations  
522 of aerosols and cloud-induced wind should be added to factors that need to be considered  
523 or improved to better parameterize warm cumulus clouds and their interactions with  
524 aerosols.

525

526

527

528

529

530

531

532

533

534

535

536

537

538

539

540

541

542

543

544

545

546

547 **Code/Data source and availability**

548

549 Our private computer system stores the code/data which are private and used in this study.  
550 Upon approval from funding sources, the data will be opened to the public. Projects related  
551 to this paper have not been finished, thus, the sources prevent the data from being open to  
552 the public currently. However, if information on the data is needed, contact the  
553 corresponding author Seoung Soo Lee (slee1247@umd.edu).

554

555 **Author contributions**

556 Essential initiative ideas are provided by SSL, JU and WJC to start this work. Simulation  
557 and observation data are analyzed by SSL, JU and KJH. CHJ, JG and YZ review the results  
558 and contribute to their improvement.

559

560 **Competing interests**

561 The authors declare that they have no conflict of interest.

562

563

564

565

566

567

568

569

570

571

572

573

574

575

576

577

578

579

580

581

582

583

584

585

586

**587 Acknowledgements**

588

589 This study is supported by the National Research Foundation of Korea (NRF) grant funded  
590 by the Korea government (MSIT) (No. NRF2020R1A2C1003215 and No.  
591 2020R1A2C1013278) and the Korea Institute of Marine Science and Technology  
592 Promotion(KIMST) funded by the Ministry of Oceans and Fisheries (20210607). This  
593 study is also supported by Basic Science Research Program through the NRF funded by  
594 the Ministry of Education (No. 2020R1A6A1A03044834), FRIEND (Fine Particle  
595 Research Initiative in East Asia Considering National Differences) project through the  
596 NRF, funded by the Ministry of Science and ICT (grant no. 2020M3G1A1114617) and  
597 National Research Foundation of Korea (NRF) grant, funded by the Korean government  
598 (NRF-2021R1F1A1046878).

599

600

601

602

603

604

605

606

607

608

609

610

611

612

613

614

615

616

617

618 **References**

619

620 Albrecht, B. A.: Aerosols, cloud microphysics, and fractional cloudiness, *Science*, 245,  
621 1227-1230, 1989.

622 Brown, A., Milton, S., Cullen, M., Golding, B., Mitchell, J., and Shelly, A.: Unified  
623 modeling and prediction of weather and climate: A 25-year journey, *Bull. Am*  
624 *Meteorol. Soc.* 93, 1865–1877, 2012.

625 Chaboureau, J.-P., Labbouz, L., Flamant, C., and Hodzic, A.: Acceleration of the southern  
626 African easterly jet driven by the radiative effect of biomass burning aerosols and its  
627 impact on transport during AEROCLO-sA, *Atmos. Chem. Phys.*, 22, 8639–8658,  
628 <https://doi.org/10.5194/acp-22-8639-2022>, 2022.

629 Che, H., Stier, P., Watson-Parris, D., Gordon, H., and Deaconu, L.: Source attribution of  
630 cloud condensation nuclei and their impact on stratocumulus clouds and radiation in  
631 the south-eastern Atlantic, *Atmos. Chem. Phys.*, 22, 10789–10807,  
632 <https://doi.org/10.5194/acp-22-10789-2022>, 2022.

633 Chen, F., and Dudhia, J.: Coupling an advanced land-surface hydrology model with the  
634 Penn State-NCAR MM5 modeling system. Part I: Model description and  
635 implementation, *Mon. Wea. Rev.*, 129, 569–585, 2001.

636 de Graaf, M., Bellouin, N., Tilstra, L.G., Haywood, J., Stammes, P.: Aerosol direct radiative  
637 effect of smoke over clouds over the southeast Atlantic Ocean from 2006 to 2009.  
638 *Geophys. Res. Lett.* 41, 7723-7730, 2014.

639 Deaconu, L. T., Ferlay, N., Waquet, F., Peers, F., Thieuleux, F., and Goloub, P.: Satellite  
640 inference of water vapour and above cloud aerosol combined effect on radiative  
641 budget and cloud top processes in the southeastern Atlantic Ocean, *Atmos. Chem.*  
642 *Phys.*, 19, 11613–11634, <https://doi.org/10.5194/acp-19-11613-2019>, 2019.

643 Denjean, C., Bourriane, T., Burnet, F., Mallet, M., Maury, N., Colomb, A., Dominutti, P.,  
644 Brito, J., Dupuy, R., Sellegri, K., Schwarzenboeck, A., Flamant, C., and Knippertz, P.:  
645 Overview of aerosol optical properties over southern West Africa from DACCIIWA  
646 aircraft measurements, *Atmos. Chem. Phys.*, 20, 4735–4756,  
647 <https://doi.org/10.5194/acp-20-4735-2020>, 2020.

648 Feingold, G., H. Jiang, H., and J. Y. Harrington, J. Y.: On smoke suppression of clouds in

- 649 Amazonia, *Geophys. Res. Lett.*, 32, L02804, doi:10.1029/2004GL021369, 2005.
- 650 Forster, P., et al., Changes in atmospheric constituents and in radiative forcing, in: *Climate*  
651 *change 2007: the physical science basis, Contribution of working group I to the Fourth*  
652 *Assessment Report of the Intergovernmental Panel on Climate Change*, edited by  
653 Solomon, S., et al., Cambridge Univ. Press, New York, 2007.
- 654 Formenti, P., B. D'Anna, C. Flamant, et al.: The Aerosols, Radiation and Clouds in  
655 Southern Africa Field Campaign in Namibia: Overview, illustrative observations, and  
656 way forward, *Bull. Amer. Meteor. Soc.*, 100, 1277-1298, 2019.
- 657 Hahn, C. J., and Warren, S. G.: A gridded climatology of clouds over land (1971–96) and  
658 ocean (1954–97) from surface observations worldwide. Numeric Data Package NDP-  
659 026EORNL/CDIAC-153, CDIAC, Department of Energy, Oak Ridge, TN, 2007.
- 660 Hansen, J. E., Sato, M. and Ruedy, R.: Radiative forcing and climate response, *J. Geophys.*  
661 *Res.*, 102, 6831–6864, 1997.
- 662 Hartmann, D. L., Ockert-Bell, M. E., and Michelsen, M. L.: The effect of cloud type on  
663 earth's energy balance—Global analysis, *J. Climate*, 5, 1281–1304, 1992.
- 664 Haslett, S. L., Taylor, J. W., Evans, M., Morris, E., Vogel, B., Dajuma, A., Brito, J.,  
665 Batenburg, A. M., Borrmann, S., Schneider, J., Schulz, C., Denjean, C., Bourriane,  
666 T., Knippertz, P., Dupuy, R., Schwarzenböck, A., Sauer, D., Flamant, C., Dorsey, J.,  
667 Crawford, I., and Coe, H.: Remote biomass burning dominates southern West African  
668 air pollution during the monsoon, *Atmos. Chem. Phys.*, 19, 15217–15234,  
669 <https://doi.org/10.5194/acp-19-15217-2019>, 2019.
- 670 Haywood, J. M. and Shine, K. P.: Multi-spectral calculations of the radiative forcing of  
671 tropospheric sulfate and soot aerosols using a column model, *Q. J. R. Meteorol. Soc.*,  
672 123, 1907–1930, 1997.
- 673 Holben, B. N., Tanré, D., Smirnov, et al.: An emerging ground-based aerosol climatology:  
674 Aerosol optical depth from AERONET, *J. Geophys. Res.*, 106, 12067–12097, 2001.
- 675 Johnson, B. T., Shine, K. P., and Forster, P. M.: The semi-direct aerosol effect: Impact of  
676 absorbing aerosols on marine stratocumulus, *Q. J. R. Meteorol. Soc.*, 130, 1407– 1422,  
677 2004.
- 678 Khain, A., Pokrovsky, A., Rosenfeld, D., Blahak, U., and Ryzhkoy, A.: The role of CCN in  
679 precipitation and hail in a mid-latitude storm as seen in simulations using a spectral

- 680 (bin) microphysics model in a 2D dynamic frame, *Atmos. Res.*, 99, 129–146, 2011.
- 681 Lee, S. S., Guo, J. M., and Li, Z.: Delaying precipitation by air pollution over the Pearl  
682 River Delta. Part II: Model simulations, *J. Geophys. Res.*, 121, 11739–11760.
- 683 Lee, S. S., Ha, K.-J., Manoj, M. G., et al.: Midlatitude mixed-phase stratocumulus  
684 clouds and their interactions with aerosols: how ice processes affect microphysical,  
685 dynamic, and thermodynamic development in those clouds and interactions?, *Atmos.*  
686 *Phys. Chem.*, 21, 16843–16868, 2021.
- 687 Mari, C. H., Cailley, G., Corre, L., Saunois, M., Attié, J. L., Thouret, V., and Stohl, A.:  
688 Tracing biomass burning plumes from the Southern Hemisphere during the AMMA  
689 2006 wet season experiment, *Atmos. Chem. Phys.*, 8, 3951–3961,  
690 <https://doi.org/10.5194/acp-8-3951-2008>, 2008.
- 691 McFarquhar, G. M. and Wang, H.: Effects of Aerosols on Trade Wind Cumuli over the  
692 Indian Ocean: Model Simulations, *Q. J. R. Meteorol. Soc.*, 132, 821–843, 2006.
- 693 Menut, L., Flamant, C., Turquety, S., Deroubaix, A., Chazette, P., and Meynadier, R.:  
694 Impact of biomass burning on pollutant surface concentrations in megacities of the  
695 Gulf of Guinea, *Atmos. Chem. Phys.*, 18, 2687–2707, [https://doi.org/10.5194/acp-18-](https://doi.org/10.5194/acp-18-2687-2018)  
696 [2687-2018](https://doi.org/10.5194/acp-18-2687-2018), 2018.
- 697 Mlawer, E. J., Taubman, S. J., Brown, P. D., Iacono, M. J., and Clough, S. A.: RRTM, a  
698 validated correlated-k model for the longwave, *J. Geophys. Res.*, 102, 16663–16668,  
699 1997.
- 700 Ramaswamy, V., et al.: Radiative forcing of climate change, in *Climate Change 2001: The*  
701 *Scientific Basis*, edited by J. T. Houghton et al., 349–416, Cambridge Univ. Press,  
702 New York, 2001.
- 703 Redemann, J., Wood, R., Zuidema, P., et al.: An overview of the ORACLES (ObseRvations  
704 of Aerosols above CLouds and their intEractionS) project: aerosol–cloud–radiation  
705 interactions in the southeast Atlantic basin, *Atmos. Chem. Phys.*, 21, 1507–1563, 2021.
- 706 Roberts, G. C. and Nenes, A.: A Continuous-Flow Streamwise Thermal-Gradient CCN  
707 Chamber for Atmospheric Measurements, *Aerosol Sci. Technol.*, 39, 206–221  
708 <https://doi.org/10.1080/027868290913988>, 2005.
- 709 Stephens, G. L., and Greenwald, T. J.: Observations of the Earth’s radiation budget in  
710 relation to atmospheric hydrology. Part II: Cloud effects and cloud feedback. *J.*

- 711 Geophys. Res., 96, 15 325–15 340, 1991.
- 712 Tao, W.-K., Chen, J.-P., Li, Z., Wang, C., and Zhang C., Impact of aerosols on convective  
713 clouds and precipitation, *Rev. Geophys.*, 50, RG2001, doi:10.1029/2011RG000369,  
714 2012.
- 715 Twomey, S.: The influence of pollution on the shortwave albedo of clouds, *J. Atmos. Sci.*,  
716 34, 1149-1152, 1977.
- 717 Twomey, S.: Pollution and the Planetary Albedo, *Atmos. Env.*, 8, 1251-1256, 1974.
- 718 van der Werf, G. R., Randerson, J. T., Giglio, L., Collatz, G. J., Mu, M., Kasibhatla, P. S.,  
719 Morton, D. C., DeFries, R. S., Jin, Y., and van Leeuwen, T. T.: Global fire emissions  
720 and the contribution of deforestation, savanna, forest, agricultural, and peat fires  
721 (1997–2009), *Atmos. Chem. Phys.*, 10, 11707–11735, [https://doi.org/10.5194/acp-10-](https://doi.org/10.5194/acp-10-11707-2010)  
722 11707-2010, 2010.
- 723 Wang, H., Skamarock, W. C., and Feingold, G.: Evaluation of scalar advection schemes in  
724 the Advanced Research WRF model using large-eddy simulations of aerosol-cloud  
725 interactions, *Mon. Wea. Rev.*, 137, 2547-2558, 2009.
- 726 Warren, S. G., Hahn, C. J., London, J., Chervin, R. M., and Jenne, R. L.: Global distribution  
727 of total cloud cover and cloud types over land. NCAR Tech. Note NCAR/TN-  
728 273+STR, National Center for Atmospheric Research, Boulder, CO, 29 pp. + 200  
729 maps, 1986.
- 730 Wilcox, E. M.: Stratocumulus cloud thickening beneath layers of absorbing smoke aerosol,  
731 *Atmos. Chem. Phys.*, 10, 11769–11777, <https://doi.org/10.5194/acp-10-11769-2010>,  
732 2010.
- 733 Wood, R.: Stratocumulus clouds, *Mon. Wea. Rev.*, 140, 2373-2423, 2012.
- 734 Xu, H., Guo, J., Wang, Y., et al.: Warming effect of dust aerosols modulated by overlapping  
735 clouds below, *Atmos. Env.*, 166, 2017, 393-402, 2017.
- 736
- 737
- 738
- 739
- 740
- 741
- 742
- 743



744 **FIGURE CAPTIONS**

745

746 Figure 1. (a) An inner rectangle in the map of the Korean Peninsula represents the  
747 simulation domain. The green represents the land area and the light blue the ocean area in  
748 the map. A black dot marks the location of a site where the radiosonde sounding is obtained  
749 and a red dot the location of the PM<sub>2.5</sub> station in the Yellow sea. (b) The simulation domain  
750 is shown. The black dots mark the locations of the PM<sub>2.5</sub> stations and the red dot the location  
751 of the AERONET site in the domain.

752

753 Figure 2. Spatial distribution of cloud reflectivity which is unitless and observed by the  
754 COMS at 14:00 LST April 13<sup>th</sup>, 2016 in the simulation domain. Contours are at 0.11, 0.15,  
755 0.19 and 0.25.

756

757 Figure 3. Vertical distributions of potential temperature and water-vapor mixing ratio at  
758 09:00 LST on April 13<sup>th</sup>, 2016. These distributions are obtained from radiosonde sounding  
759 near the simulation domain in Figure 1a.

760

761 Figure 4. Time series of PM<sub>2.5</sub> observed at the station in the Yellow sea (blue line) and of  
762 the average PM<sub>2.5</sub> over stations in the simulation domain (red line) between 03:00 LST and  
763 18:00 LST on April 13<sup>th</sup> in 2016.

764

765 Figure 5. Aerosol size distribution at the surface. N represents aerosol number  
766 concentration per unit volume of air and D represents aerosol diameter.

767

768 Figure 6. Same as Figure 2 but in the control run.

769

770 Figure 7. Vertical distributions of the time- and area-averaged cloud-liquid mass density  
771 that represents cloud mass for the standard simulations (i.e., the control, aro-above-cld,  
772 control-1500 and aro-above-cld-1500 runs).

773

774 Figure 8. Time series of the domain-averaged (a) liquid-water path, (b) updraft speed, (c)  
775 condensation rate and (d) CAPE in the standard simulations.

776 Figure 9. Vertical distributions of the time- and area-averaged radiative heating rate (a) in  
777 the control and aro-above-cld runs over the initial period between 10:00 and 13:50 LST,  
778 (b) in the control and aro-above-cld runs and (c) in the control-1500 and aro-above-cld-  
779 1500 runs over the whole simulation period.

780

781 Figure 10. Vertical distributions of the time- and area-averaged aerosol concentrations (a)  
782 in the control and control-novary runs, (b) aro-above-cld and aro-above-cld-novary runs,  
783 (c) control-1500 and control-novary-1500 runs and (d) aro-above-cld-1500 and aro-above-  
784 cld-novary-1500 runs.

785

786 Figure 11. Vertical distributions of the time- and area-averaged cloud-liquid mass density.  
787 In (a), the control-novary, aro-above-cld-novary, control-1500-novary and aro-above-cld-  
788 1500-novary runs and in (b), the control-norad, aro-above-cld-norad, control-1500-norad  
789 and aro-above-cld-1500-norad runs are shown together with the standard simulations.

790

791

792

793

794

795

796

797

798

799

800

801

802

803

804

805

Simulations	Altitudes of a aerosol layer (km)	Aerosol concentrations in the aerosol layer at the first time step ( $\text{cm}^{-3}$ )	Aerosol evolution	Aerosol radiative effects
Control	0 - 1	15000	Present	Present
Aro-above-cld	2.5-3.5	15000	Present	Present
Control-1500	0 - 1	1500	Present	Present
Aro-above-cld-1500	2.5-3.5	1500	Present	Present
Control-novary	0 - 1	15000	Absent	Present
Aro-above-cld-novary	2.5-3.5	15000	Absent	Present
Control-1500-novary	0 - 1	1500	Absent	Present
Aro-above-cld-1500-novary	2.5-3.5	1500	Absent	Present
Control-norad	0 - 1	15000	Present	Absent
Aro-above-cld-norad	2.5-3.5	15000	Present	Absent
Control-1500-norad	0 - 1	1500	Present	Absent
Aro-above-cld-1500-norad	2.5-3.5	1500	Present	Absent

806

807 Table 1. Summary of simulations

808

809

810

811

812

813

814

815

816

817

818

819

Simulations	Net solar radiation flux reaching the surface (W m <sup>-2</sup> )	Surface latent heat fluxes (W m <sup>-2</sup> )	Surface sensible heat fluxes (W m <sup>-2</sup> )	Surface latent heat fluxes plus surface sensible heat fluxes (W m <sup>-2</sup> )
Control	293 (205)	175 (120)	22 (16)	197 (136)
Aro-above-cld	306 (217)	170 (117)	48 (33)	218 (150)
Control-1500	461	250	70	320
Aro-above-cld-1500	467	248	75	323

820

821 Table 2. The time- and area-averaged net solar radiation, latent heat, sensible heat and total  
822 heat (sensible plus latent heat) fluxes at the surface over the whole simulation period in the  
823 standard simulations. Numbers in the parentheses are averaged over the initial period  
824 between 10:00 and 13:50 LST for the control and aro-above-cld runs.

825

826

827

828

829

830

831

832

833

834

835

836

837

838

839

840

841

	Control run	Observations	Observation sources
Cloud fraction (CF)	0.25	0.21	Ground stations
Cloud-top height (CTH) (km)	2.8	2.6	COMS
Cloud-bottom height (CBH) (km)	1.1	1.0	Ground stations
Cloud optical depth (COD)	3.5	3.2	The Moderate Resolution Imaging Spectroradiometer (MODIS)
Droplet effective radius ( $r_e$ ) ( $\mu\text{m}$ )	7.5	8.0	MODIS
Liquid-water path (LWP) ( $\text{g m}^{-2}$ )	17.3	16.8	MODIS
The surface wind speed (WS) ( $\text{m s}^{-1}$ )	1.8	1.6	Ground stations
The surface wind direction (WD) (Degree; measured clockwise from geographical north)	220	230	Ground stations
The surface air temperature (ST) (Degree Celsius)	16.9	16.7	Ground stations

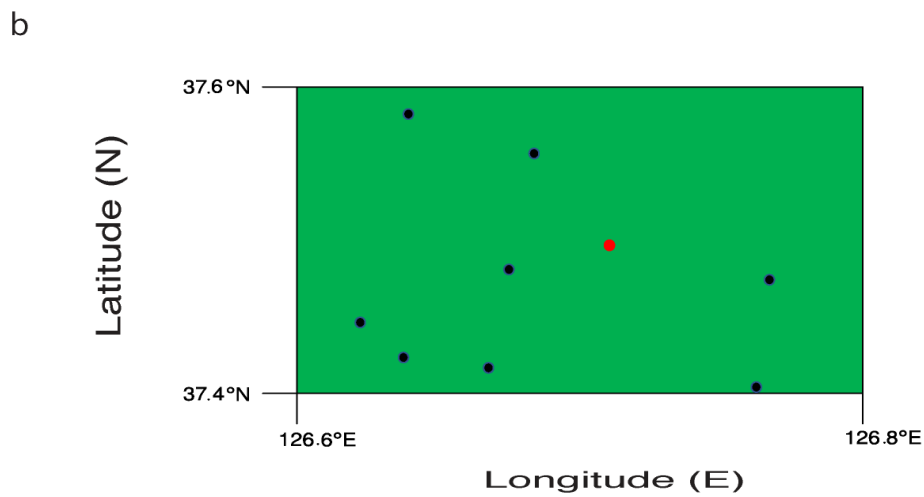
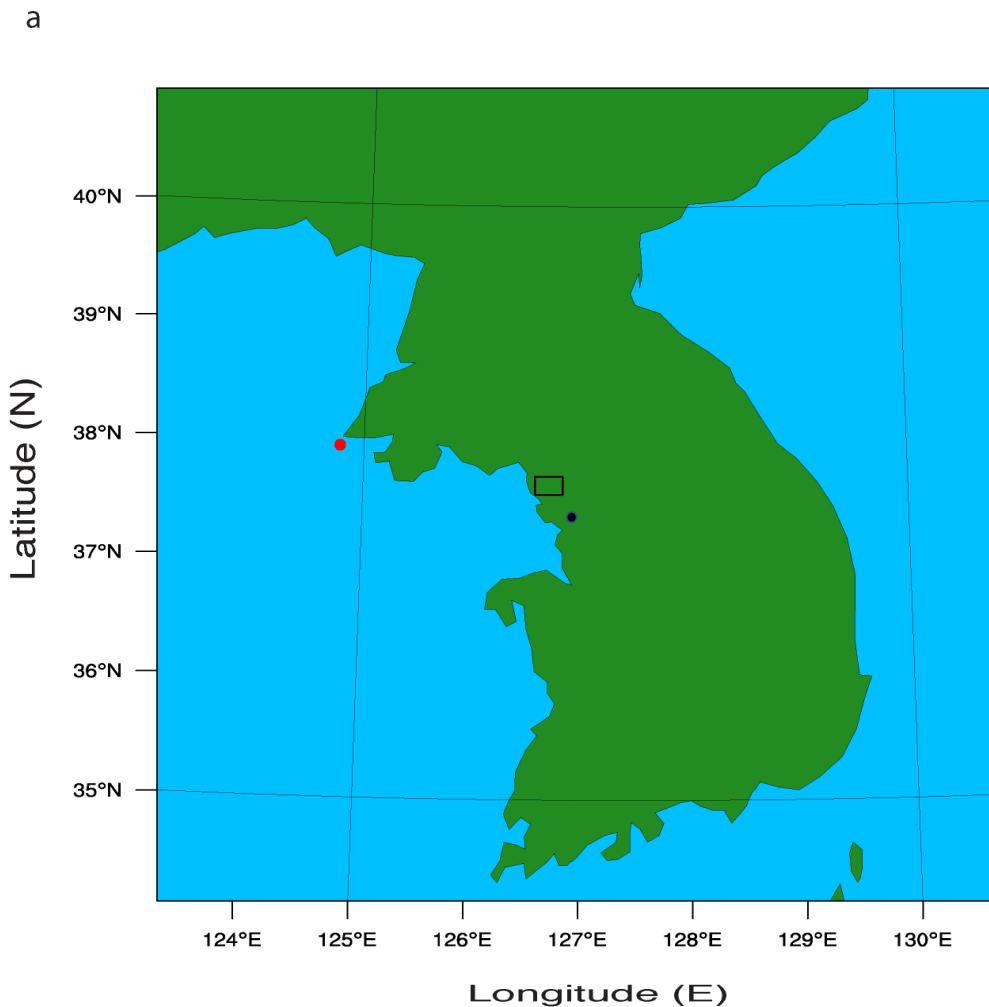
842

843 Table 3. The simulated and observed values of cloud and environmental variables, and the  
844 observation sources that have been used to obtain the observed values. At each observation  
845 time (simulation time step), CF is averaged (obtained) over ground stations (grid points) in  
846 the domain as shown in Figure 1b and the averaged (obtained) CF is averaged over the

847 simulation period with clouds to calculate the presented and observed (simulated) CF  
848 values. To obtain the presented values of CTH, CBH, COD,  $\tau_e$  and LWP, the observed  
849 values at observation spatial points (the simulated values in grid columns for CTH, CBH  
850 and LWP and at grid points for COD and  $\tau_e$ ) in the domain are averaged over areas with  
851 non-zero values at each observation time (simulation time step) and then over the  
852 simulation period with non-zero values. To obtain the presented values of WS, WD and  
853 ST, the simulated values at grid points, which correspond to the atmosphere immediately  
854 above the surface, and each simulation time step, and the observed values at ground stations  
855 and each observation time are averaged over the domain and then over the whole  
856 simulation period.

857

858

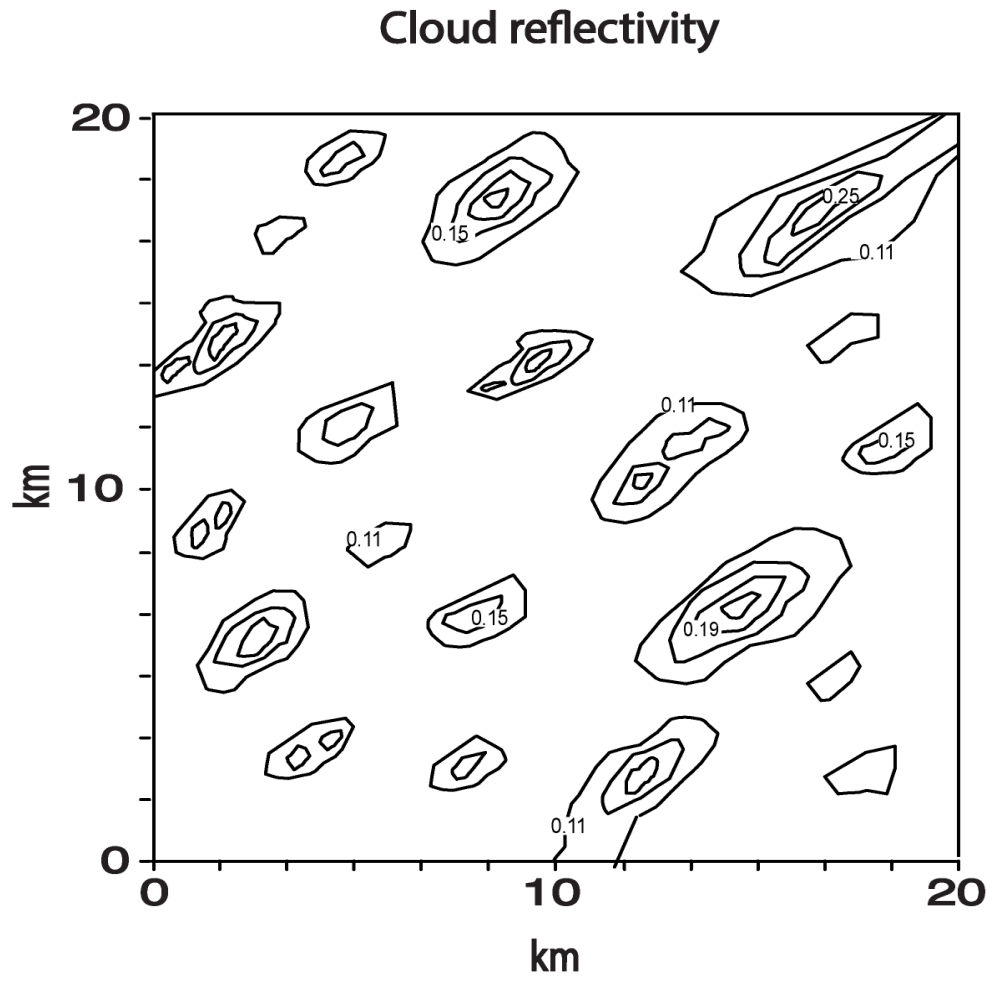


859

860

861

**Figure 1**



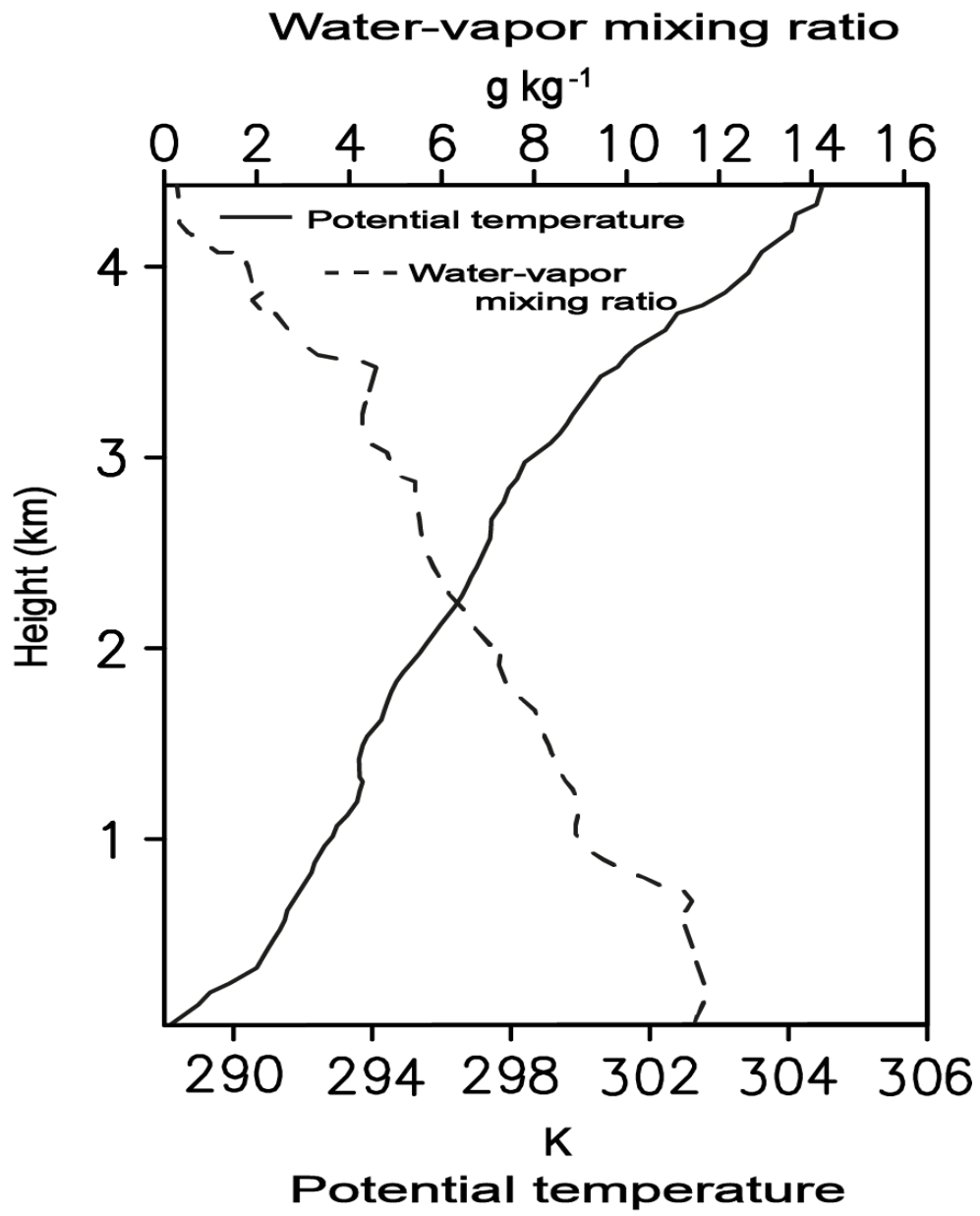
862

863

**Figure 2**

864





865

866

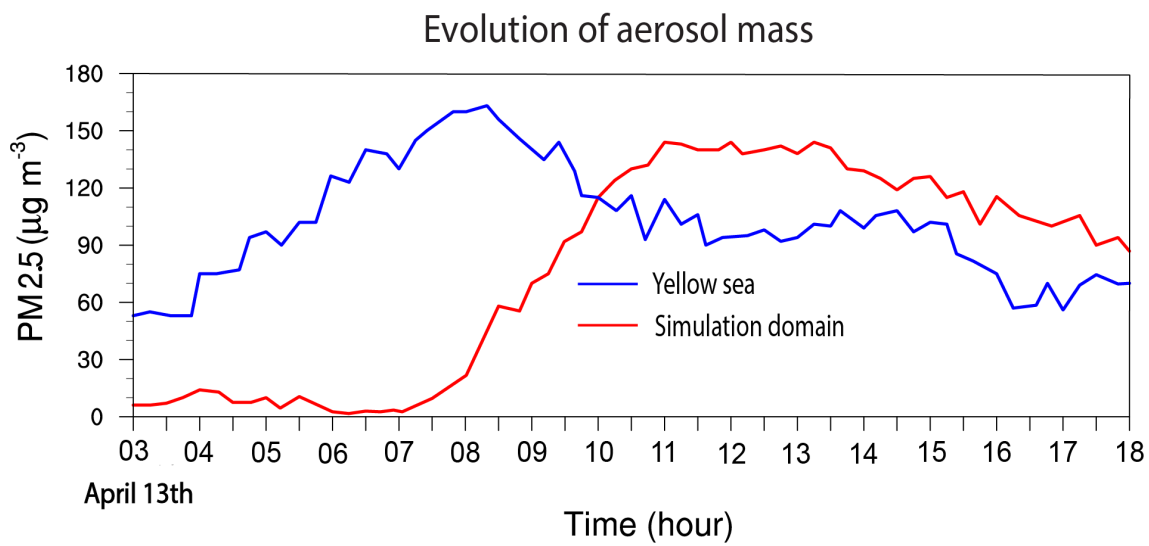
867

868

869

870

**Figure 3**



871

872

**Figure 4**

873

874

875

876

877

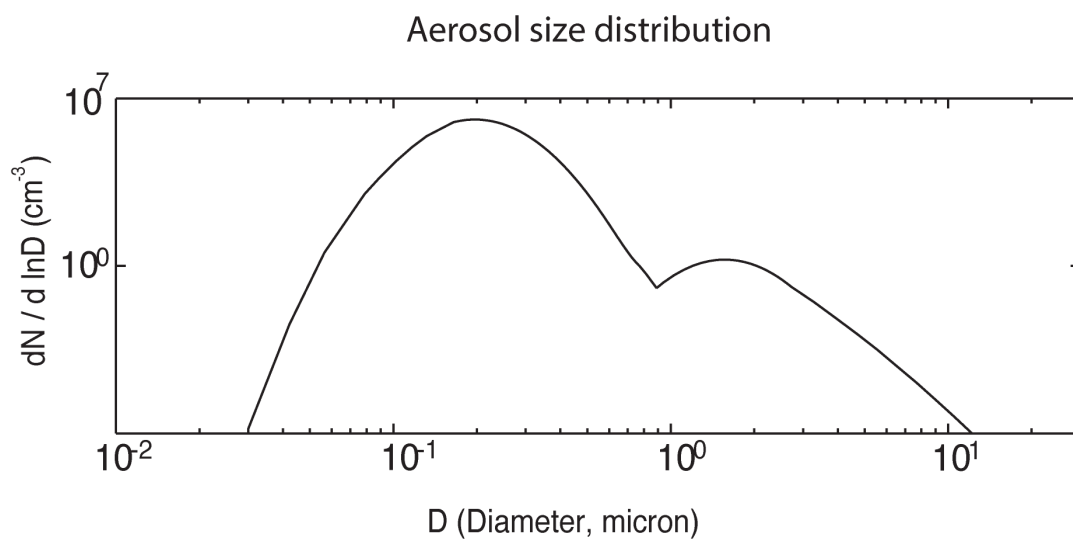
878

879

880

881

882



883

884

**Figure 5**

885

886

887

888

889

890

891

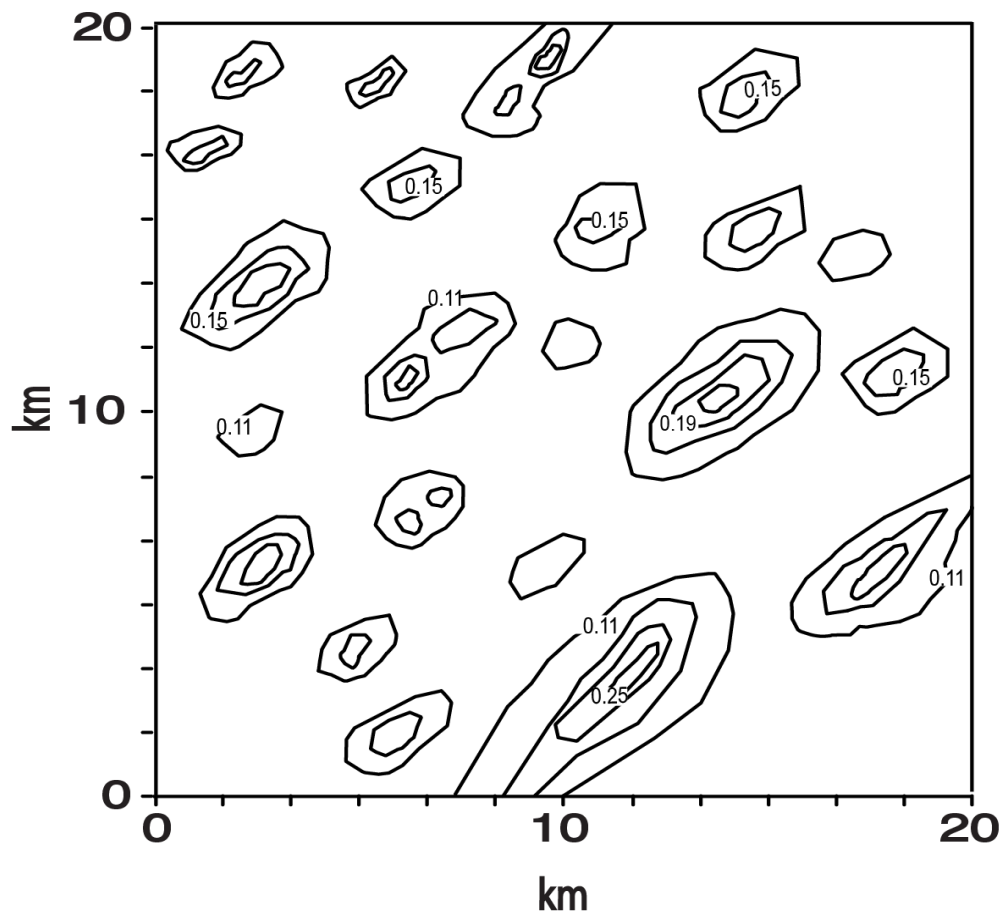
892

893

894

895

## Cloud reflectivity



896

897

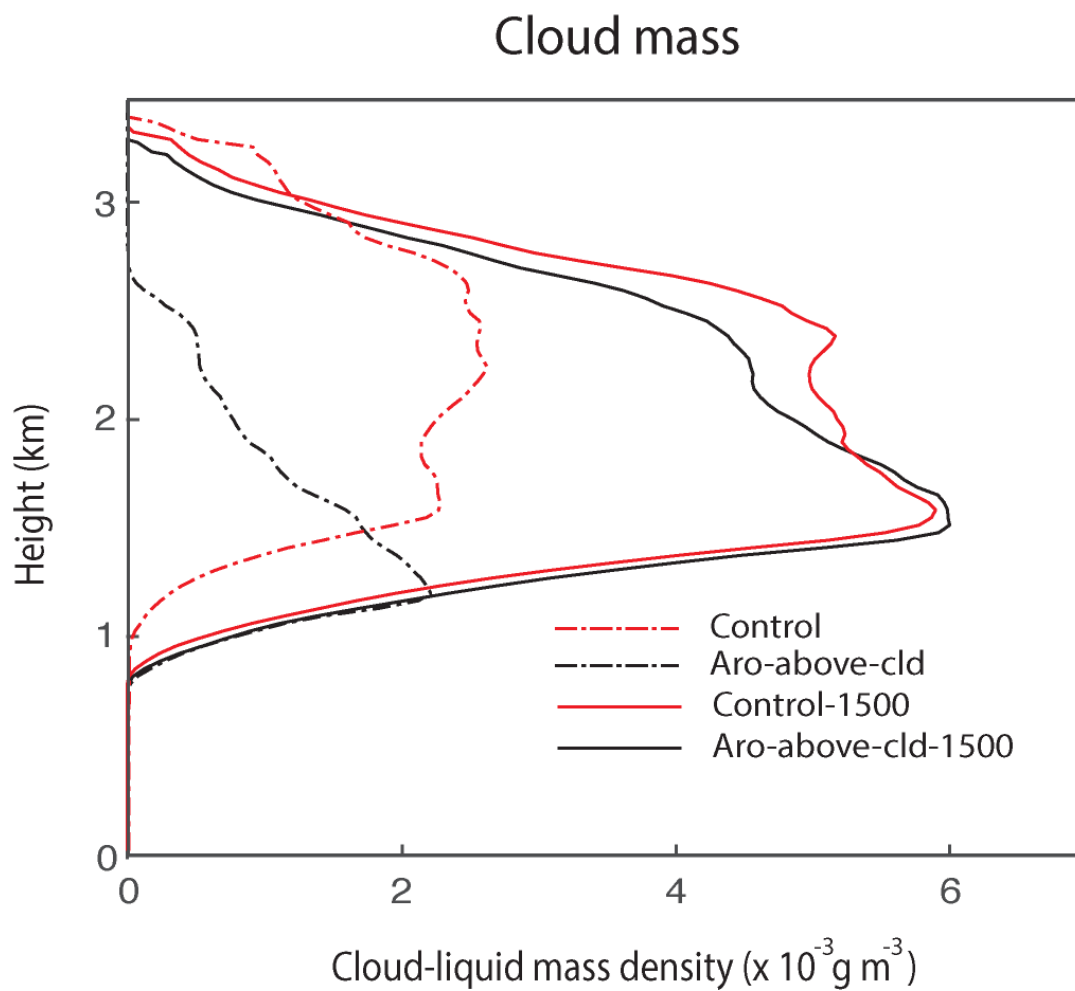
898

899

900

901

**Figure 6**



902

903

904

905

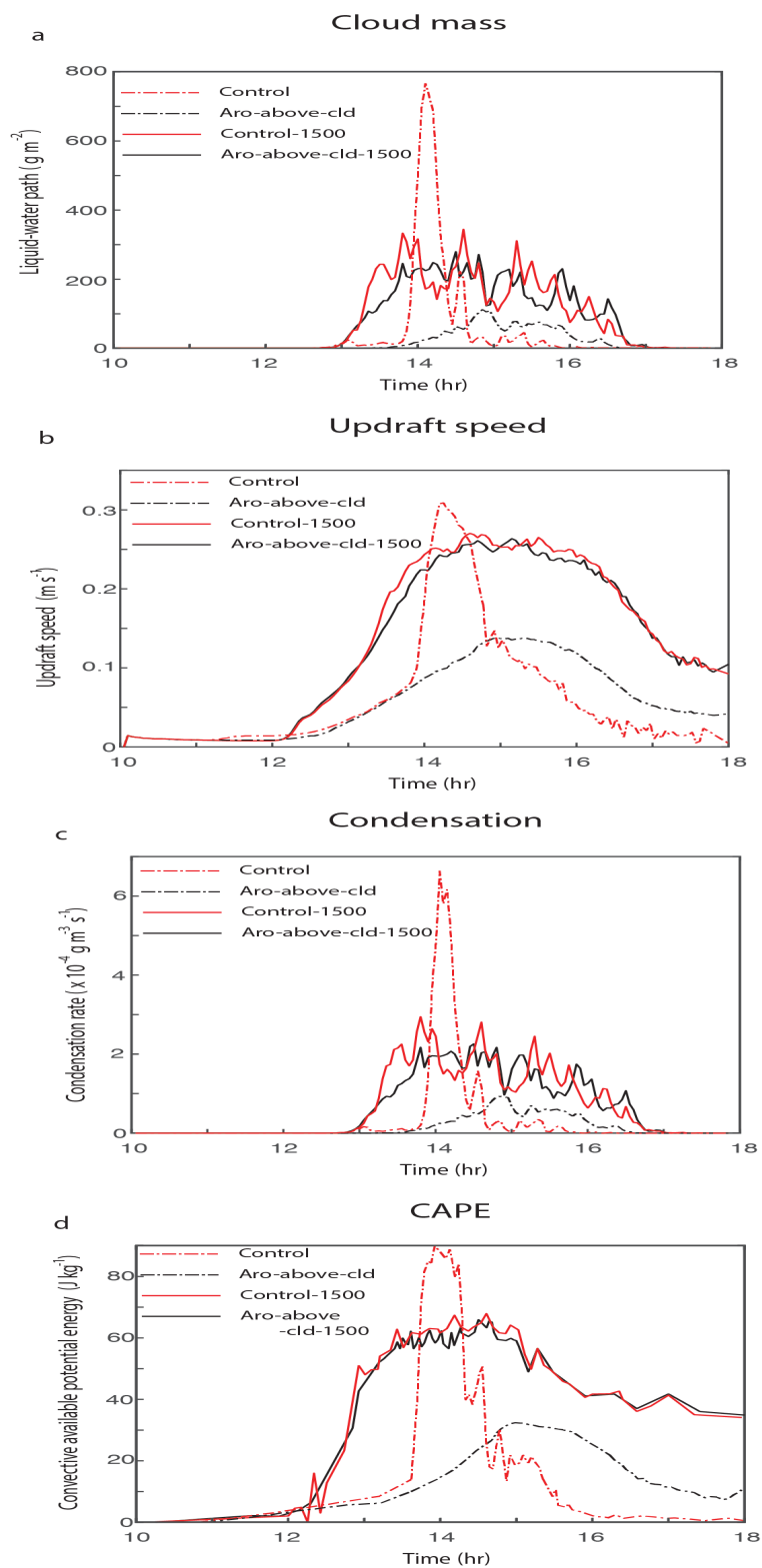
906

907

908

909

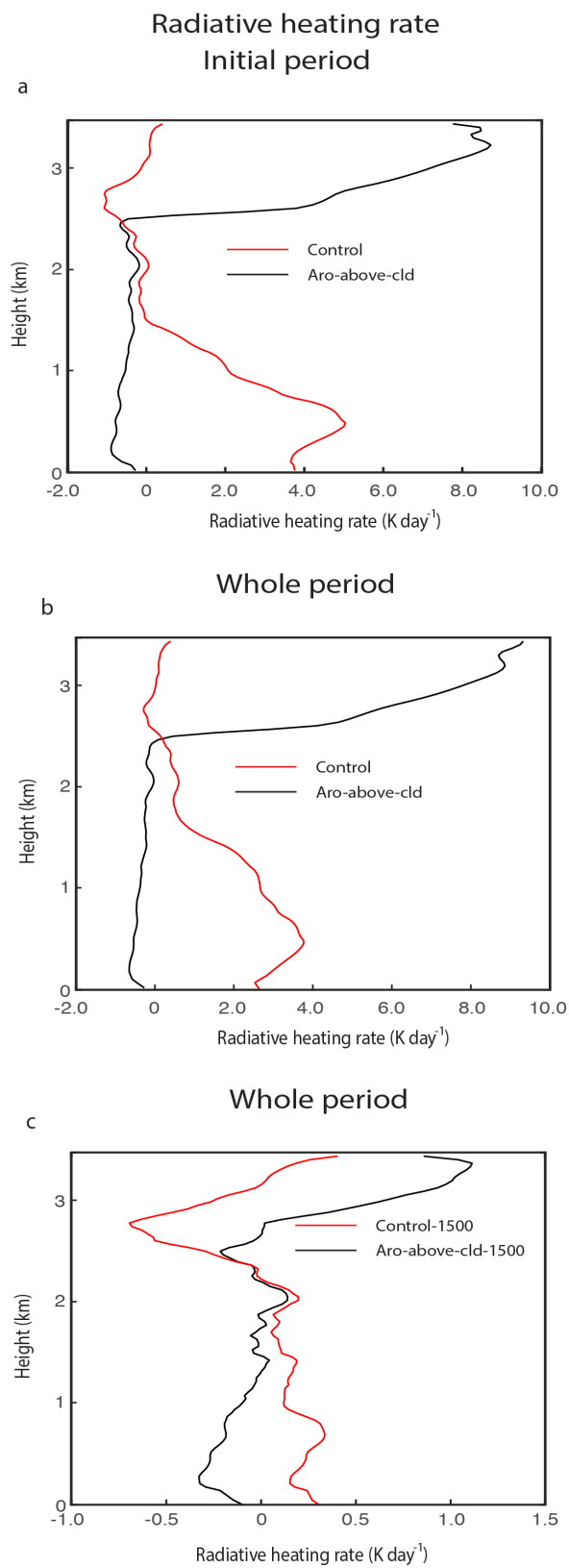
**Figure 7**



910

911

Figure 8



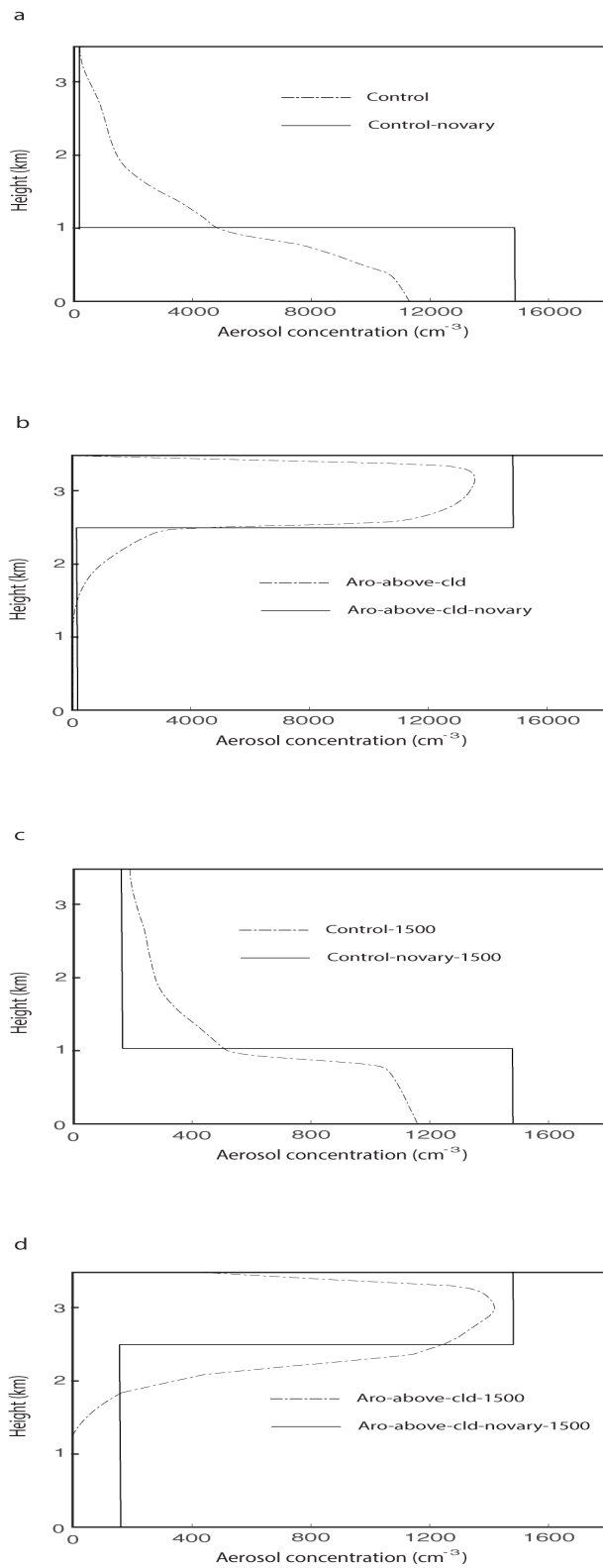
912

913

914

**Figure 9**

## Vertical distributions of aerosol concentrations



915

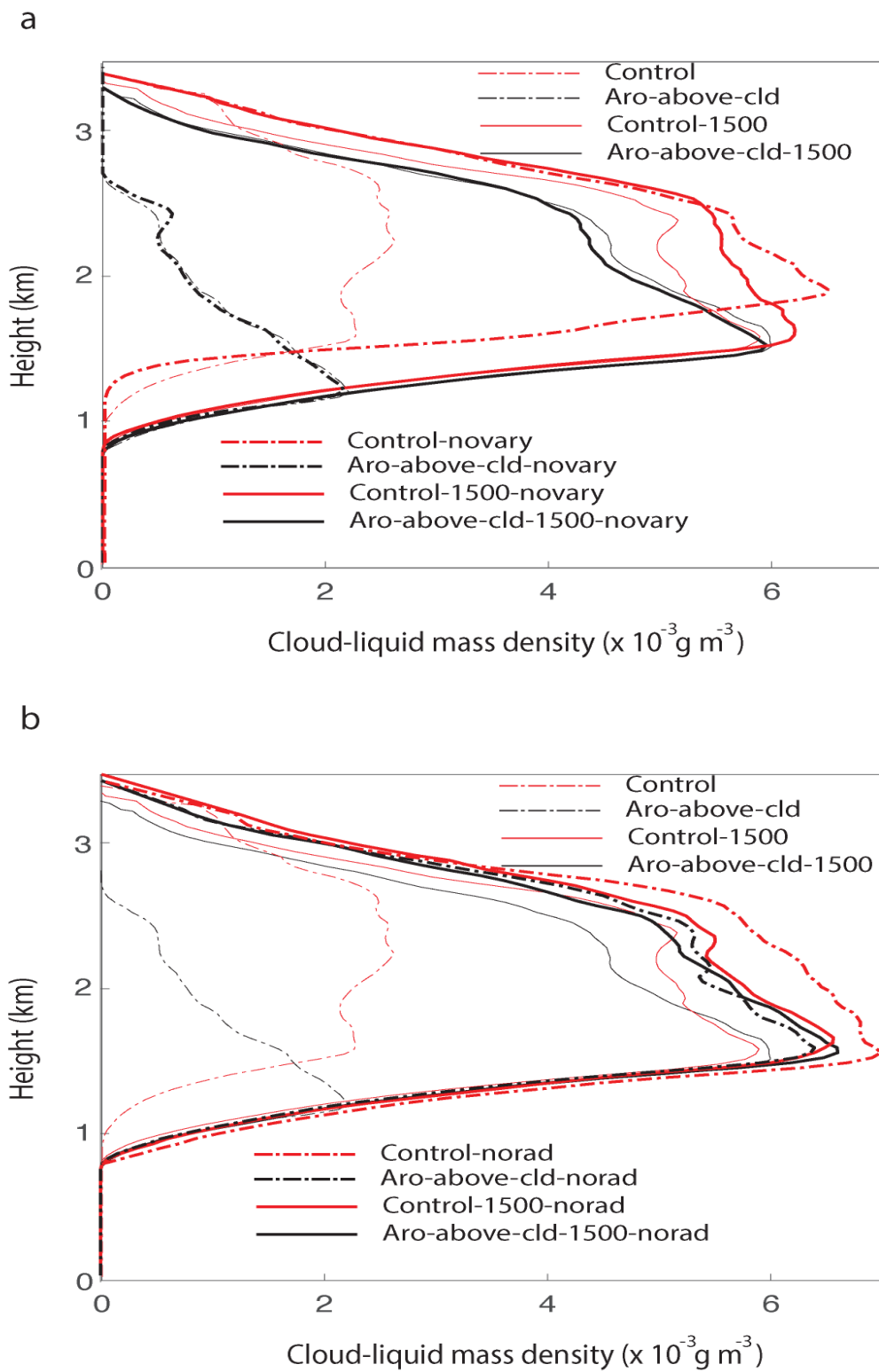
916

917

Figure 10



## Cloud mass



918

919

920

**Figure 11**